Modeling of Ship Effluent Transport and Its Sensitivity to Boundary Layer Structure

QINGFU LIU, YEFIM L. KOGAN, AND DOUGLAS K. LILLY

Cooperative Institute for Mesoscale Meteorological Studies, University of Oklahoma, Norman, Oklahoma

DOUGLAS W. JOHNSON

Meteorological Research Flight, The Met. Office, Farnborough, Hampshire, United Kingdom

GEORGE E. INNIS

Science Applications International Corporation, San Diego, California

PHILIP A. DURKEE AND KURT E. NIELSEN

Department of Meteorology, Naval Postgraduate School, Monterey, California

(Manuscript received 9 July 1996, in final form 26 October 1998)

ABSTRACT

The LES model is applied for studying ship track formation under various boundary layer conditions observed during the Monterey Area Ship Track experiment. Simulations in well-mixed and decoupled boundary layers show that ship effluents are easily advected into the cloud layer in the well-mixed convective boundary layer, whereas their transport may be suppressed by the subcloud transitional layer in the decoupled case. The clear difference between the well-mixed and decoupled cases suggests the important role of diurnal variation of solar radiation and consequent changes in the boundary layer stability for ship track formation. The authors hypothesize that, all other conditions equal, ship track formation may be facilitated during the morning and evening hours when the effects of solar heating are minimal.

In a series of experiments, the authors also studied the effects of additional buoyancy caused by the heat from the ship engine exhaust, the strength of the subcloud transitional layer, and the subcloud layer saturation conditions. The authors conclude that additional heat from ship engine and the increase in ship plume buoyancy may indeed increase the amount of the ship effluent penetrating into the cloud layer. The result, however, depends on the strength of the stable subcloud transitional layer. Another factor in the ship effluent transport is the temperature of the subcloud layer. Its decrease will result in lowering the lifting condensation level and increased ship plume buoyancy. However, the more buoyant plumes in this case have to overcome a larger potential barrier. The relation between all these parameters may be behind the fact that ship tracks sometimes do, and sometimes do not, form in seemingly similar boundary layer conditions.

1. Introduction

The role of atmospheric aerosol particles is clearly illustrated by studies showing the apparent sensitivity of marine stratocumulus cloud layers to anthropogenic addition of heat, smoke, and water vapor by ship passages forming ship condensation trails. The latter are commonly observed by satellite, and may last for hundreds of kilometers and many hours. These trails are reported (Radke et al. 1988) to be visually thickened and brightened parts of sometimes rather thin cloud layers (Fig. 1). The ship tracks are generally believed to be the result of a large increase in condensation nuclei in a region relatively devoid of them, thereby producing a more reflective and perhaps more durable cloud of many small droplets (Albrecht 1989). The relationship between the concentration of cloud condensation nuclei (CCN) and brightness is apparently nonlinear, as there is some evidence that intersecting condensation trails are no brighter than either trail alone (Porch et al. 1989).

Ship tracks are observed in well-mixed, as well as in decoupled, boundary layers (BLs). Material released in a well-mixed BL can be easily transported throughout the boundary layer depth in a relatively short period of time, whereas the stable *subcloud transitional layer* (STL) in the decoupled case may limit its transport. While the diffusion in the well-mixed BL has been thor-

Corresponding author address: Dr. Yefim L. Kogan, Cooperative Institute for Mesoscale Meteorological Studies, University of Oklahoma, 100 E. Boyd, Norman, OK 73019.
E-mail: ykogan@ou.edu

© 2000 American Meteorological Society

Unauthenticated | Downloaded 09/14/24 02:12 PM UTC

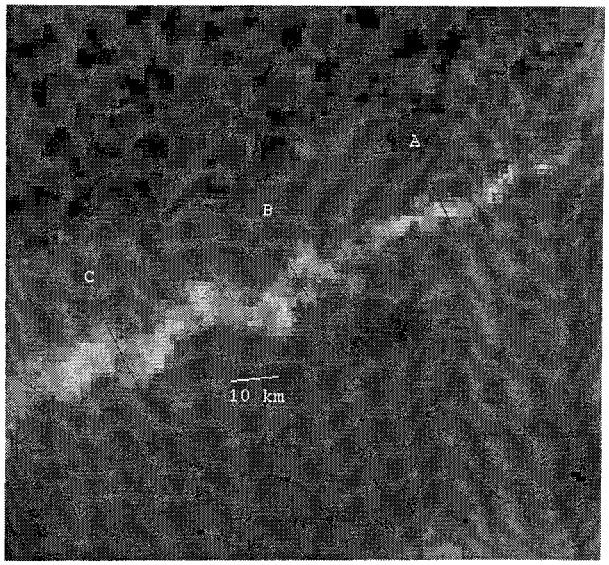

FIG. 1. Near-infrared satellite image (channel 3.55–3.93 μm) of the part of eastern Pacific at 1727 UTC on 29 Jun 1994. The ship track produced by the ship Hanjin *Barcelona* is seen a bright line of clouds going from southwest to northeast corner of the satellite image.

oughly studied since the pioneering work of Deardorff and Willis (1975) (see review in Lamb 1982), the transport of material in the decoupled BL has been studied less extensively and the results are usually case dependent. In addition to the BL stability, other parameters, such as surface heat and moisture flux, solar radiation, buoyancy associated with the ship effluent, and the stability of the STL, can also affect ship track formation and its duration. This was evident in observations made during the Monterey Area Ship Track (MAST) field program, which provided evidence that two ships moving in the same area may have different effect on ship track formation. As will be shown in the paper, the rather subtle differences in the ship track buoyancy combined with the differences in the subcloud layer parameters may significantly affect the ship effluent transport.

The present paper describes results from a modeling study that focuses on the thermodynamical BL parameters that control transport of ship effluent into the cloud layer. These include BL stability, ship track buoyancy affected by fuel burning, and subcloud saturation conditions. A brief description of the Cooperative Institute for Mesoscale Meteorological Studies (CIMMS) large eddy simulation (LES) model used in the study is given in section 2. The transport of ship effluent in well-mixed and decoupled boundary layers is investigated in section 3 using the bulk microphysical version of the model. Section 4 is a brief summary of the main points of this study.

2. CIMMS LES cloud model

The governing equations for the resolved velocity field are the grid-averaged Navier–Stokes and continuity equations for incompressible fluid in the Boussinesq approximation (Khairoutdinov and Kogan 1999):

$$\frac{\partial \overline{u}_i}{\partial t} = -\frac{\partial}{\partial x_j}(\overline{u}_j\overline{u}_i + \delta_{ij}\theta_{v0}\pi' + \tau_{ij}) + \delta_{i3}g\frac{\overline{\theta_v'}}{\theta_{v0}} + \varepsilon_{ij3}f(\overline{u}_j - u_{gj}) - w_s\frac{\partial \overline{u}_i}{\partial z} \quad (1)$$

$$\frac{\partial \overline{u}_i}{\partial x_i} = 0, \quad (2)$$

where $\overline{u}_i$ ($i = 1, 2, 3$) are the resolved-scale velocity components; δ_{ij} is the Kronecker delta symbol; ε_{ijk} is the permutation tensor; u_{gj} ($j = 1, 2$) are the geostrophic velocity components; π is the Exner function defined as $\pi = C_p(p/p_0)^{R/C_p}$; τ_{ij} ($i, j = 1, 2, 3$) are the subgrid-scale Reynolds stresses; f is the Coriolis parameter; C_p is the specific heat of the air at constant pressure; w_s is the large-scale subsidence rate; θ_v is the virtual potential temperature defined as $\theta_v = \theta_l + (L/C_p)q_l$; g is the gravity acceleration; θ_l is the virtual liquid water potential temperature; and p_0 and θ_{v0} are the reference pressure and virtual potential temperature, respectively. Bars over individual variables represent the resolved-scale quantities, while variables with primes are deviations from their horizontal mean.

The thermodynamic state is described in terms of the virtual liquid water potential temperature $\theta_l = h_l/C_p$ and the total water mixing ratio $q_t = q_v + q_l$. The virtual liquid water static energy (Emanuel 1994) h_l is defined as $h_l = C_pT(1 + 0.61q_v - q_l) + gz - L_{ql}$, where q_v is the water vapor mixing ratio and q_l is the liquid water content. Both θ_l and q_t are conserved following an air parcel in moist adiabatic processes. The governing equations for the virtual liquid water potential temperature and the total water mixing ratio are

$$\frac{\partial \overline{\theta}_l}{\partial t} = -\frac{\partial}{\partial x_j}(\overline{u}_j\overline{\theta}_l + \overline{u_j'\theta_l'}) + \frac{L}{C_p}\frac{\partial Q_p}{\partial z} - w_s\frac{\partial \overline{\theta}_l}{\partial z} + \left(\frac{\partial \overline{\theta}_l}{\partial t}\right)_{\text{rad}} + s_\theta \quad (3)$$

$$\frac{\partial \overline{q}_t}{\partial t} = -\frac{\partial}{\partial x_j}(\overline{q}_t\overline{u}_j + \overline{u_j'q_t'}) - \frac{\partial Q_p}{\partial z} - w_s\frac{\partial \overline{q}_t}{\partial z}, \quad (4)$$

where Q_p is the precipitation flux; and $\overline{u_j'\theta_l'}$ and $\overline{u_j'q_t'}$ are the subgrid-scale (SGS) fluxes of θ_l and q_t, respectively. The terms with Q_p account for the vertical divergence of precipitation flux. The third term in (3) and (4) represents the effect of large-scale vertical advection, which is calculated as $w_s = -\nabla \cdot z$, where ∇ is a constant large-scale divergence specified as an external parameter. The last two terms on the right-hand side of (3) represent heating or cooling due to shortwave and longwave radiation and the source term due to ship engine heat, respectively.

The Reynolds stresses and the SGS fluxes are as-

Unauthenticated | Downloaded 09/14/24 02:12 PM UTC

sumed to be proportional to the local gradients of the resolved-scale quantities (Lilly 1962),

$$\tau_{ij} = -k_m\left(\frac{\partial \overline{u}_i}{\partial x_j} + \frac{\partial \overline{u}_j}{\partial x_i}\right) \tag{5}$$

$$\overline{u_j'\varphi'} = -k_h\left(\frac{\partial \overline{\varphi}}{\partial x_j}\right), \tag{6}$$

where φ represents thermodynamic variables; and k_m and k_h are the eddy viscosity and eddy conductivity coefficients, respectively. The coefficients are determined by one-and-a-half-order SGS closure proposed by Lilly (1962) and further developed and applied in LES by Deardorff (1980). The closure is based on the prognostic equation for the SGS turbulent kinetic energy (TKE) $e \equiv 0.5(\overline{u_i u_i} - \overline{u_i}\,\overline{u_i})$,

$$\frac{\partial e}{\partial t} = -\frac{\partial}{\partial x_j}\left(e\overline{u}_j - 2k_m\frac{\partial e}{\partial x_j}\right) + \frac{1}{2}\left|\left(\frac{\partial \overline{u}_i}{\partial x_j} + \frac{\partial \overline{u}_j}{\partial x_i}\right)\right|^2 - k_h N^2 - \frac{C_\varepsilon e^{3/2}}{l}, \tag{7}$$

where l is the subgrid length scale, N is the Brunt–Väisälä frequency, and C_ε is a nondimensional constant. The coefficients k_m and k_h are defined as

$$k_m = C_k l\sqrt{e} \qquad k_h = \left(1 + 2\frac{l}{\Delta}\right)k_m,$$

where $\Delta = (\Delta x\, \Delta y\, \Delta z)^{1/3}$ is a characteristic grid size.

The boundary conditions are essentially the same as those of Moeng (1984) except that we impose a Galilean transformation and move the model domain at a constant speed (U_t, V_t). In the moving coordinate system, the sea surface is moving at the same speed but in the opposite direction ($-U_t$, $-V_t$). Therefore, the components ($-U_t$, $-V_t$) need to be added to the resolved-scale wind components in the surface flux calculations. The top and bottom boundaries are rigid ($w = 0$), which implies that all resolved-scale vertical fluxes vanish there, and the vertical transport of momentum and tracer quantities is done solely by the SGS fluxes.

Microphysical and radiative processes

The CIMMS LES model has two different formulations of microphysical processes, an explicit one based on the prediction of the CCN and drop size spectra and a bulk one in which liquid water content (LWC) is diagnostically determined from the θ_l and q_t (Moeng 1986). For the present study, which focuses on effects of various BL parameters on the ship effluent (SE) transport from a surface source, the bulk microphysical approach is both adequate and economical. The SE transport was emulated by predicting the evolution of the passive tracer field. The governing equation for the passive tracer concentration, c, is

$$\frac{\partial \overline{c}}{\partial t} = -\frac{\partial}{\partial x_j}(\overline{c}\,\overline{u}_j + \overline{u_j'c'}) - w_s\frac{\partial \overline{c}}{\partial z} + s_c, \tag{8}$$

where s_c is the source term describing the SE release and $\overline{u_j'c'}$ describes the SGS tracer flux defined similar to (6).

The longwave and shortwave radiation fluxes and the associated heating and cooling rates are calculated using the broadband radiative transfer code developed by Wyant et al. (1997). Tests performed by C. Bretherton (1996, personal communication) show that the solar heating rates calculated by the broadband code agree with the 24-band Slingo and Schrecker (1982) code with an error less than 5%.

The finite-difference discretization is based on the staggered Arakawa C grid. The advective transport of momentum is computed using a flux-conserving advection scheme analogous to Tremback et al.'s (1987) with an option to select the order of spatial accuracy from the second to the fifth. The advection of scalar variables (including TKE, thermodynamic variables, and microphysical variables) is calculated using the three-dimensional positive definite and nonoscillatory version of the Smolarkiewicz and Grabowski (1990) advection scheme. The time integration is performed using the third-order Adams–Bashforth scheme.

The simulations were made in a domain of 64 × 64 × 40 grid points for the well-mixed case and 64 × 64 × 50 grid points for the decoupled case using a time step of 4 s. The grid sizes in both cases are $\Delta x = \Delta y = 100$ m, and $\Delta z = 20$ m.

3. Effects of the boundary layer structure on the ship track formation

We evaluate the dispersion rate of the SE by simulating transport of a passive tracer from a surface source under two different stratocumulus BL conditions: one well-mixed and another decoupled from the surface by a stable STL. In the decoupled case, we will also analyze the effect of heat released by the ship engine on the ship track formation. The simulations are based on the bulk microphysical version of the CIMMS LES model and are initialized using soundings obtained by the U.K. Meteorological Research Flight C-130 airplane on 8 June 1994 (case A334, sounding P1) and on 29 June 1994 (case A348). The two ship tracks simulated in our study are formed by ships Hyundai *Duke* (A334) and Hanjin *Barcelona* (A348). Both ships are heading in the direction of 118°. The ship speed is $U_{\text{ship}} = 12.6$ m s^{-1} for Hyundai *Duke* and $U_{\text{ship}} = 7.7$ m s^{-1} for Hanjin *Barcelona.* The model's horizontal coordinates are rotated 28° clockwise in both cases so that the x direction is parallel to the ship path. The geostrophic wind components in this new coordinate system are $U_g = 10.1$ m s^{-1}, $V_g = -8.2$ m s^{-1} in the A334 case and $U_g = 5.2$ m s^{-1}, $V_g = 9.7$ m s^{-1} in the A348 case.

The surface heat flux is fixed at 12.0 W m^{-2} in A334

Unauthenticated | Downloaded 09/14/24 02:12 PM UTC

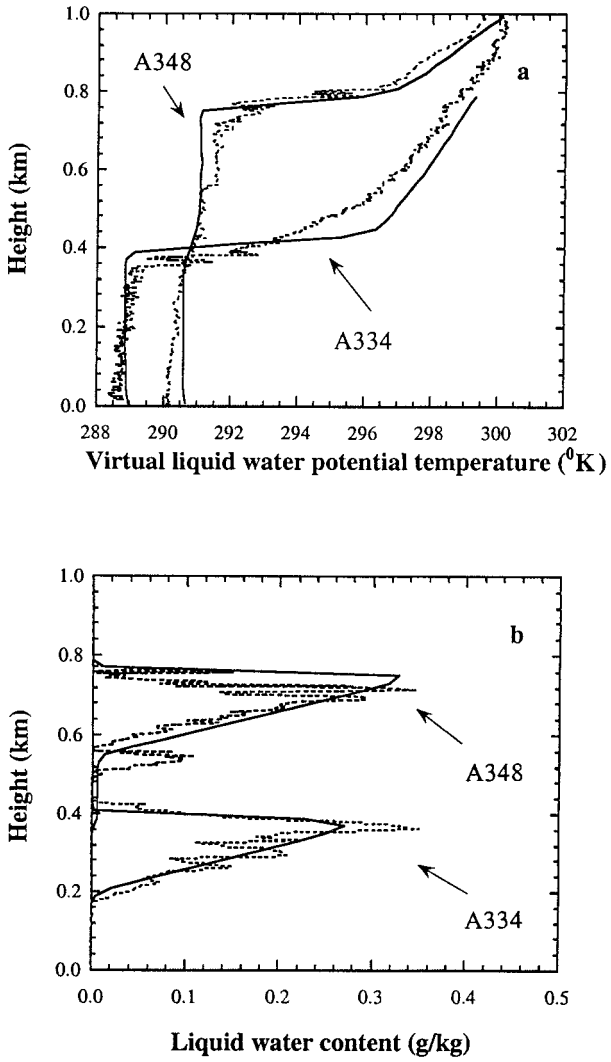

FIG. 2. Vertical profiles of (a) virtual liquid water potential temperature and (b) liquid water content for the A334 and A348 cases. Dashed lines show the observational data; solid lines show model results at 2 h into simulation.

and at 10.0 W m^{-2} in A348. The surface moisture flux is calculated based on the surface heat flux and the thermodynamic variables at the 10-m height (Moeng 1986). The large-scale divergence is 2.5×10^{-6} s^{-1} in both cases. The turbulence is initialized by random perturbations of virtual liquid water potential temperature with magnitude of 0.1°C. After the initialization, the model is run for 2 h in order for the turbulence to fully develop. Figure 2 shows the vertical profiles of the virtual liquid water potential temperature and liquid water content in both cases at 2 h into simulation, as well as sounding taken by the airplane. As evident from Fig. 2, the boundary layer is well mixed in the A334 case and is slightly decoupled in the A348 case. In the latter case, the BL is divided into two parts separated by an STL near 0.4 km.

There are two different approaches for modeling the SE release. In the first one, a moving point source is simulated and the SE is released each time step at the ship's current position. This approach provides a realistic description of the ship track evolution and most appropriate for studying the dispersion of the SE in the horizontal plane. However, due to the limited integration domain, the SE may be followed only for a short simulation time before it reaches the boundary. For parameters of the studied MAST cases, the SE would not penetrate deep into the cloud layer during this short time interval, thus limiting the number of points that can be used for calculating statistics on the SE concentration in the cloud. For demonstration purposes, we made a simulation of the A334 case using the point source approach and show in Fig. 3 the distribution of the SE at 35 min after its release. The SE is released at a rate of 2×10^{14} s^{-1} and is distributed uniformly over four grid cells adjacent to the ship's current position. The background concentration of the passive tracer is specified at 20 cm^{-3}. Since the governing equation (8) for the passive tracer is linear, one can apply linear operators to the passive tracer field to scale it to the observed aerosol concentrations.

The maximum concentration of the SE at 20 min after SE release ($\sim$200 cm^{-3}) is about an order of magnitude larger than the background concentration. For simplicity, in this demonstration experiment we assume that the release point moves eastward with the speed $U_{\text{ship}} - U_g = 2.5$ m s^{-1} and neglect the y component of the ship speed as it will further reduce the time before the SE will reach the domain boundary. As already mentioned, the major drawback of such simulation is that the SE reaches the model domain boundary rather quickly, in our demonstration experiment in about 25 min (Fig. 3).

A statistically more significant sample can be obtained by simulating many ship tracks released from a number of different locations and then calculating the ensemble average concentration. From practical considerations, we combine these simulations into one experiment and release the SE simultaneously along one line. More specifically, the SE is released into a rectangular box parallel to the x axis and positioned at two grid cells along the y axis (at $y = 200$ and $y = 300$ m) and two grid cells along the z axis (at $z = 10$ and $z = 30$ m). In all simulations described below, we release the SE at 2 h into simulation for 40 s; during this time the ship moving along the x axis with the speed of 2.5 m s^{-1} covers 100 m, that is, the size of one grid.

Figure 4 shows the SE distribution at 20 min after its release; both the SE concentration and the ship track width are comparable to that of the ship track from a point source shown in Fig. 3. Because of the nonzero wind component along the y axis, the ship track shifts in the north direction. However, in the line source simulation, the ship track initially aligned parallel to the x axis, after reaching the north boundary, reappears be-

Unauthenticated | Downloaded 09/14/24 02:12 PM UTC

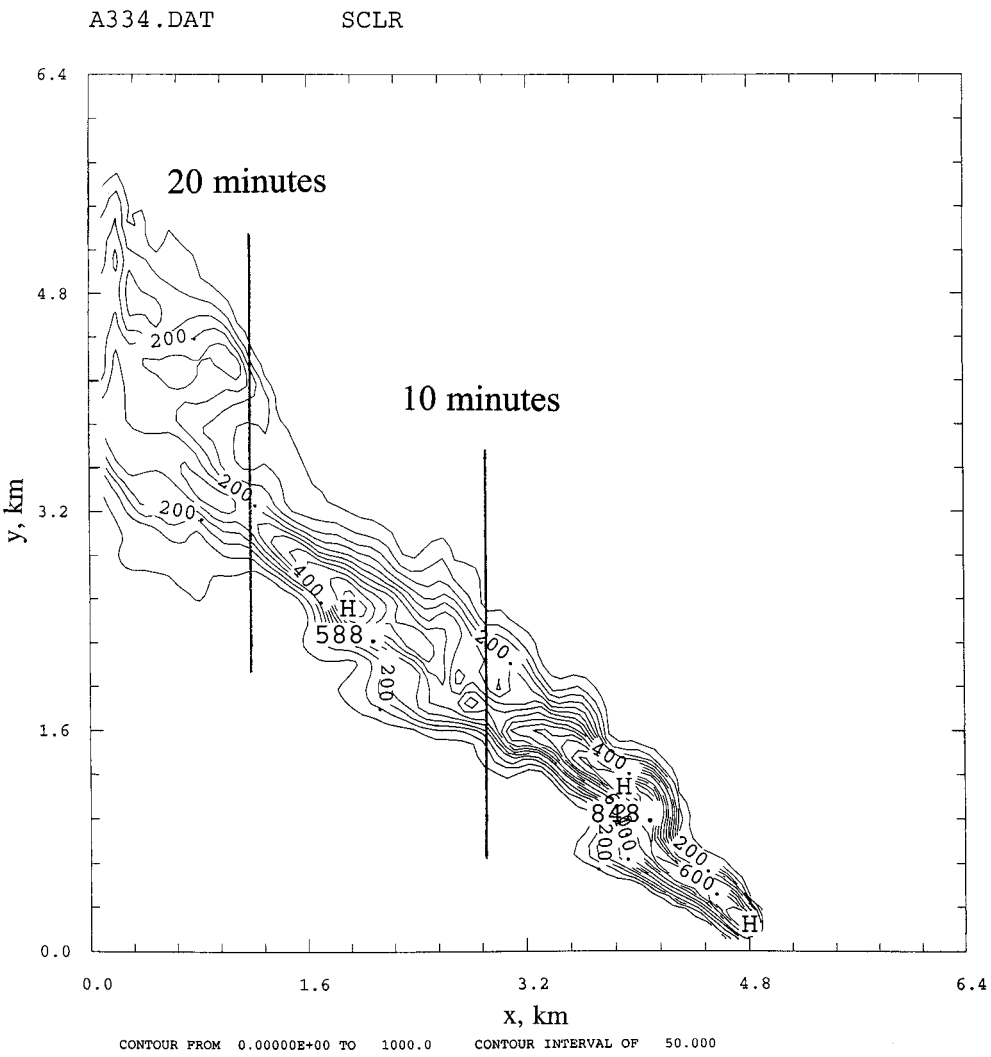

FIG. 3. Column-averaged concentration distribution of the ship effluent from a moving point source in the A334 case. The vertical lines show the ship effluent position at 10 and 20 min after release.

cause of the periodic boundary conditions at the south boundary in a confined area also parallel to the *x* axis. This allows a much longer integration time that is limited only by the time when diffusion spreads the SE over the entire horizontal domain.

a. Transport in the well-mixed versus decoupled boundary layers

A well-mixed buoyancy driven boundary layer, normally associated with strong turbulence and relatively large updrafts, can quickly transport material vertically as well as horizontally. The decoupled boundary layer, however, has a stable STL that suppresses the vertical motion and limits the amount of material reaching the cloud. Figure 5 shows the vertical profiles of the dimensionless vertical velocity variance, buoyancy flux, and passive tracer in the A334 and A348 cases, as well as corresponding observational data points. The vertical velocity scale is defined as in Moeng (1986):

$$w_{*c} = \left(\frac{g}{\theta_{v0}} \overline{w\theta_v'}|_c z_i \right)^{1/3},$$

where $\overline{w\theta_v'}|_c$ is the averaged total buoyancy flux inside the cloud layer and z_i is the boundary layer height. The value of w_{*c} in both simulations is approximately the same and equal to 0.55 m s^{-1}. The classic distinction between the well-mixed and the decoupled boundary layers is clearly demonstrated by the difference in the vertical velocity variance profile. It shows one maximum for the well-mixed BL case compared to two maxima separated by a minimum in the STL for the decoupled case. The buoyancy flux is positive throughout the mixed layer in the A334 case with a maximum in the cloud layer, whereas in the decoupled case A348 it

Unauthenticated | Downloaded 09/14/24 02:12 PM UTC

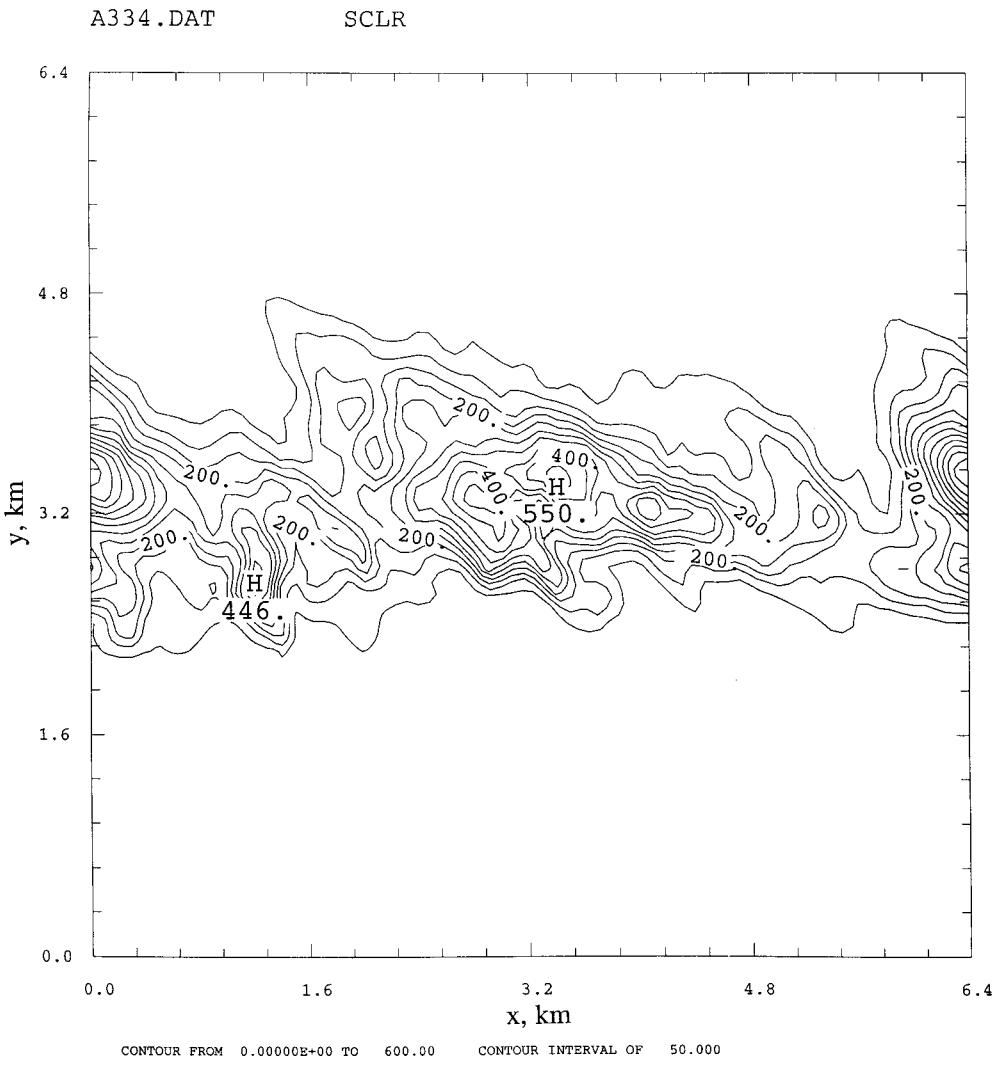

FIG. 4. Column-averaged concentration distribution of the ship effluent from a line source in the A334 case at 20 min after release.

becomes negative in the stable STL. The profiles of vertical velocity variance and buoyancy flux are in good agreement with the observational data.

In the A334 case the SE is well mixed in the boundary layer and is transported into the cloud layer in less than 20 min. In the A348 case it is mostly confined to the lower half of the boundary layer just below the STL (Fig. 5d). Analysis shows that the upward transport is dominated by large eddies with a very small contribution from the subgrid eddies. Due to the suppression of large eddies by the stable STL in the A348 case, the vertical advection of the SE is very small. This fact is illustrated by Fig. 6 showing trajectories of air parcels released along the ship track line. Consistent with Fig. 5d, almost all of the air parcels are located below the STL in the lower half of the BL. The SE exhibits a characteristic looping as plumes go up and down. Figure 7 presents isolines of the frequency distribution function that is proportional to the probability to find a ship track parcel at a particular height and time. At 35 min after its release, the SE is more or less uniformly distributed over the subcloud layer.

b. Effect of buoyancy associated with the ship engine heat

In the well-mixed case the SE easily reaches the BL top in less than 20 min (Fig. 5c). Sensitivity tests show that the additional buoyancy associated with the heat from ship engine exhaust in this case has negligible effect on the SE transport. In the decoupled case, however, the additional buoyancy due to engine heat has a more profound effect on the SE transport. Figures 8 and 9 show trajectories and the frequency distribution

Unauthenticated | Downloaded 09/14/24 02:12 PM UTC

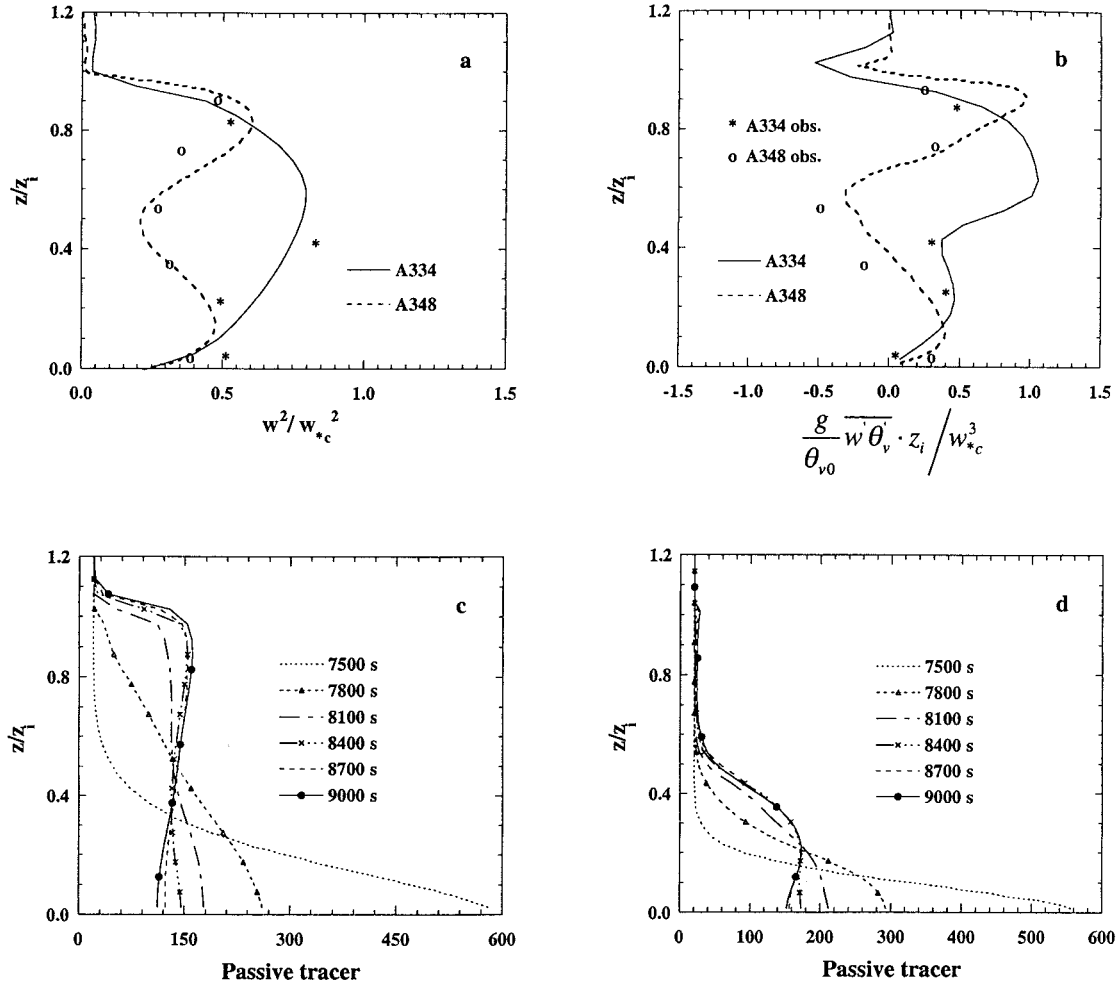

FIG. 5. Vertical profiles of the dimensionless vertical velocity variance (a) and buoyancy flux (b) in the A334 case (solid line) and A348 case (dashed line). The stars show the observational data in the A334 case, and the circles show the observational data in the A348 case. The evolution of the tracer vertical profile in cases A334 and A348 is shown in (c) and (d), respectively. The ship effluent was released as a line source at 7200 s in both cases.

function for a simulation A348_B2. This simulation is similar to A348 except for the temperature $\Delta T = 0.2$°C that was added to the SE in a manner similar to the way the SE itself was added, that is, in the same rectangular box and during the same 40-s time period. The temperature increment of $\Delta T = 0.2$°C was chosen based on the estimate of the heat energy added to the atmosphere by the Hanjin *Barcelona* ship engine (G. E. Innis 1998, personal communication). The additional buoyancy, as Figs. 8 and 9 show, results in the appearance of many thermals reaching the BL top. Of the total number of air parcels released along the ship track (1280), 300 had kinetic energy sufficient to overcome the potential barrier caused by the STL. Obviously, the more heat is added by the ship engine, the more parcels will be able to cross the STL potential barrier.

Figure 10 shows vertical profiles of dimensionless vertical velocity variance and the passive tracer concentration from three simulations: A348 (benchmark experiment), A348_B2, and A348_B1. In the latter experiment, the temperature perturbation of $\Delta T = 0.1$°C, that is, half as in A348_B2, was added to the ship track. As evident from Fig. 9a, there is no significant difference between the vertical velocity variance in all three cases, indicating that the added heat had little effect on the BL dynamics. However, the profile of the passive tracer concentration (Fig. 10b) shows an increase of the SE in the cloud layer as a result of the added ship engine heat. The latter mainly serves as a triggering mechanism that helps the most energetic thermals move across the STL into the upper cloud circulation driven by cloud radiative cooling. The STL also inhibits the momentum transport throughout the entire boundary layer depth. This results in a shift of the ship track (Fig. 8) in the upper half of the boundary layer compared to the lower half due to the differences in the horizontal velocities between these two layers (see also Figs. 11, 12).

Unauthenticated | Downloaded 09/14/24 02:12 PM UTC

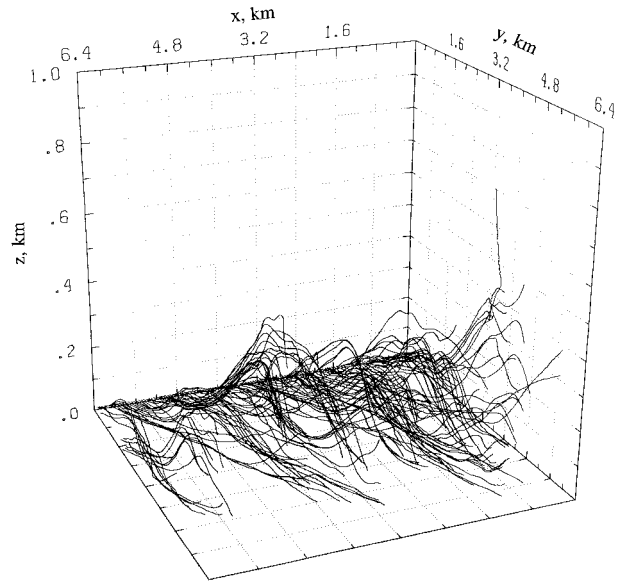

FIG. 6. Trajectories of air parcels released along the ship track. For clarity, only 128 trajectories (10%) are shown on the plot.

c. *Effect of the subcloud saturation conditions*

Other parameters that affect the ship track formation are the temperature and water vapor mixing ratio in the subcloud layer that determine the cloud condensation level. We conducted four experiments in which the virtual liquid water potential temperature below the STL was, respectively, 0.1°, 0.3°, 0.5°, and 0.7°C lower than that of the control run (A348_B1) (see Table 1). Although the temperature reduction increased the stability of STL, it, at the same time, decreased the water vapor saturation pressure. Figures 11 and 12 show vertical cross sections of the liquid water content and the passive tracer concentration (averaged along *x* direction) in simulations A348_C1 and A348_C2, respectively. It is evident that condensation in the ship track occurs at a lower level and over a wider area in A348_C2 than in A348_C1. The larger amount of latent heat released inside the ship track in the A348_C2 case results in more SE reaching the cloud layer (Figs. 11 and 12, Table 1), even though the STL in the A348_C2 case is stronger than that of the A348_C1 case. Our calculations show that there is a good correlation between the liquid water content, buoyancy force, and the vertical velocity of air parcels that penetrated into the cloud layer. The correlation coefficient between the liquid water content and the buoyancy force is 0.70 for the A348_C1 and 0.73 for the A348_C2 case. The correlation coefficient be-

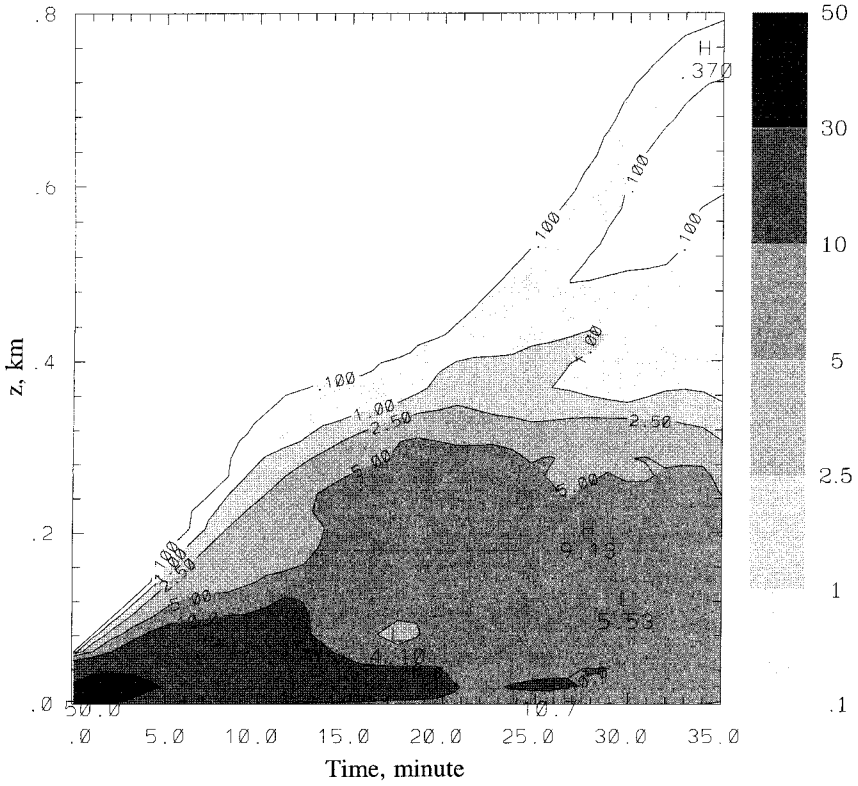

FIG. 7. Isolines of the probability (in percent) to find a ship track at a particular height and time in the A348 simulation.

Unauthenticated | Downloaded 09/14/24 02:12 PM UTC

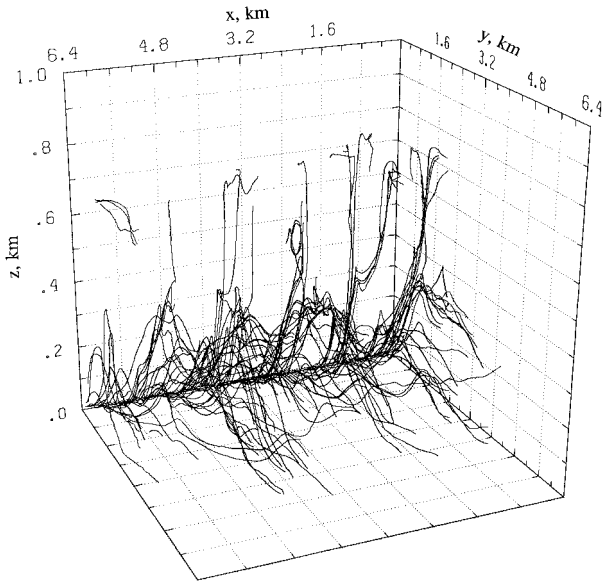

FIG. 8. Same as in Fig. 6, except for simulation A348_B2.

tween the buoyancy and the vertical velocity is 0.60 in A348_C1 and 0.71 in A348_C2. In general, parcels with higher buoyancy and larger vertical velocity are more likely to penetrate the stable STL and reach the cloud top. This is apparent from Fig. 13, which shows the amount of condensed LWC and buoyancy force in air parcels at the 400-m level. It is apparent that in the A348_C2 case, the number of parcels for any given amount of condensate or buoyancy force is increased by a factor of 2 from that in the A348_C1 case.

Figure 14 shows the percentage of the SE accumulated above the STL as a function of the stability parameter, which we define here as the temperature jump across the STL. Generally speaking, as the stability increases, the total amount of the SE above the STL decreases. However, if latent heat released inside the ship track is large enough to overcome the potential barrier imposed by the STL, the total amount of the SE penetrating into the cloud may actually increase. However, as the strength of the STL becomes too large, the transport of the SE may be completely shut off.

4. Discussion and conclusions

The LES model has been applied for studying ship track formation under two sets of boundary layer conditions observed during the Monterey Area Ship Track (MAST) experiment. We have carried out experiments simulating ship track transport produced by ships Hyundai *Duke* on 8 June 1994 in the well-mixed boundary layer and Hanjin *Barcelona* on 29 June 1994 in the

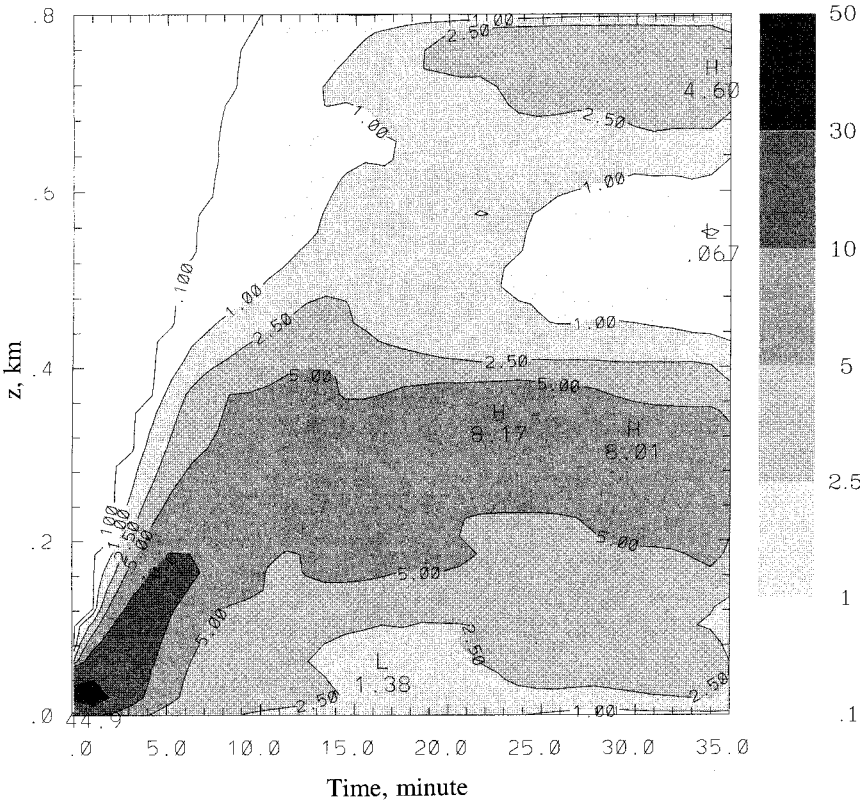

FIG. 9. Same as in Fig. 7, except for simulation A348_B2.

Unauthenticated | Downloaded 09/14/24 02:12 PM UTC

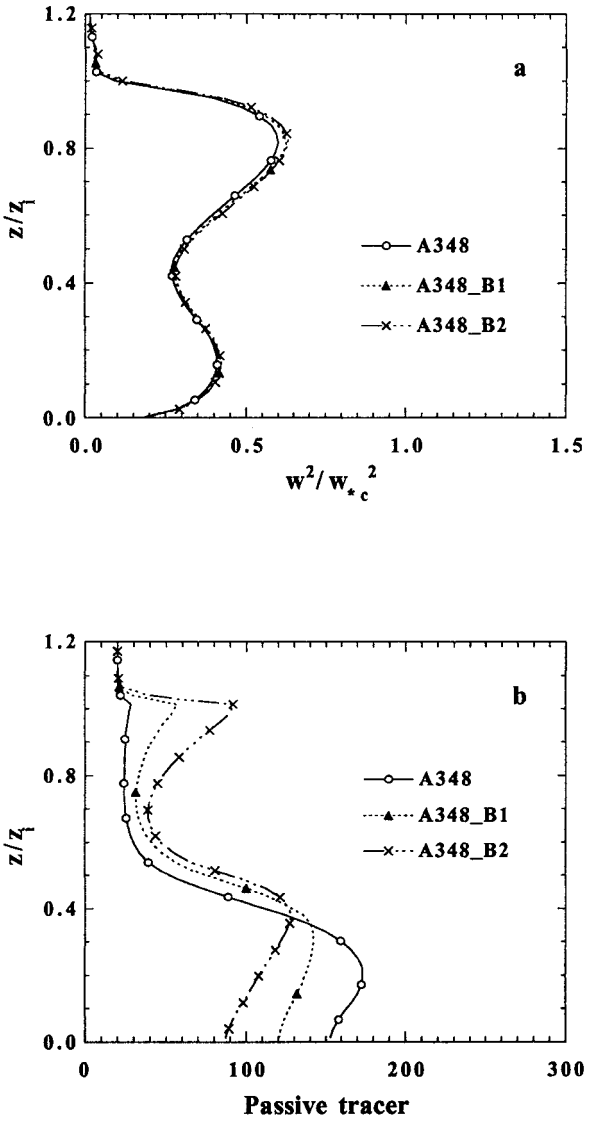

FIG. 10. Vertical profiles of the dimensionless vertical velocity variance (a) and passive tracer (b) at 30 min for simulations A348 (solid line with circles), A348_B1 (dotted line with triangles), and A348_B2 (dash-dotted line with crosses).

decoupled boundary. Although we used observational soundings from these two cases in order to initialize the model, the present investigation is not intended as a case study. Instead we are focusing on the physical mechanisms that may explain the ship effluent transport dependence on ambient conditions.

It was shown that ship effluents are easily advected into the cloud layer in the well-mixed convective boundary layer, whereas their transport may be suppressed by the subcloud transitional layer in the decoupled case. With the help of buoyancy and possibly initial momentum of the ship effluents, the most intensive convective plumes may penetrate the stable subcloud transitional layer and form a ship track in the cloud atop the boundary layer.

In a series of experiments, we also studied the effects of additional buoyancy caused by the heat from the ship engine exhaust, the strength of the subcloud transitional layer, and the subcloud layer saturation conditions. We conclude that additional heat from ship engine and the resulting increased buoyancy of the ship plume may indeed increase the amount of the ship effluent penetrating into the cloud layer. The result, however, depends on the stability of the stable subcloud transitional layer. Another factor in the ship effluent transport is the temperature of the subcloud layer. Its decrease will result in lowering the lifting condensation level and an increase in buoyancy of the ship plume due to the increase in latent heat release. However, the more buoyant plumes in this case have to overcome a larger potential barrier due to the decrease in potential temperature below the cloud deck. Clearly, the transport of ship effluent in the decoupled BL case and ship track formation is a complex phenomenon depending on the relation between different parameters characterizing plume buoyancy and boundary layer stability. The subtle change in these parameters may be behind the fact that ship tracks sometimes do, and sometimes do not, form in seemingly similar boundary layer conditions.

The demonstrated clear difference between the well-mixed and decoupled cases in the ship effluent transport suggests the important role of some other external parameters affecting the boundary layer decoupling. Among them are sea surface heat and moisture fluxes, drizzle evaporation, cloud-top radiative cooling, and solar radiative heating. The solar radiation is essential due to its role in the formation and maintenance of boundary layer decoupling. In the absence of solar heating, the initially decoupled boundary layer in our A348 simulation becomes well mixed in about an hour. The longwave radiative cooling near the cloud top increases the instability of the boundary layer and results in the development of strong convection. The vertical advection of the passive tracer is then similar to the well-mixed case. Diurnal variation of solar radiation and consequent changes in the boundary layer stability may, thus, be important in the ship track formation. We hypothesize that, all other conditions equal, ship track formation may be facilitated during the morning and evening hours when the effect of solar heating is minimal.

Another important factor in boundary layer decoupling is the surface heat flux. In our simulation of the A348 case the surface heat flux was fixed representing conditions when an air mass is moving toward a higher sea surface temperature region. As the heat is added to the lower half of the boundary layer, the temperature will increase, the stable subcloud transitional layer will erode, and more plumes will form due to the decreased stability of the inversion layer. However, if the surface temperature instead of the heat flux is kept constant, which is the case of an air mass moving over a constant

Unauthenticated | Downloaded 09/14/24 02:12 PM UTC

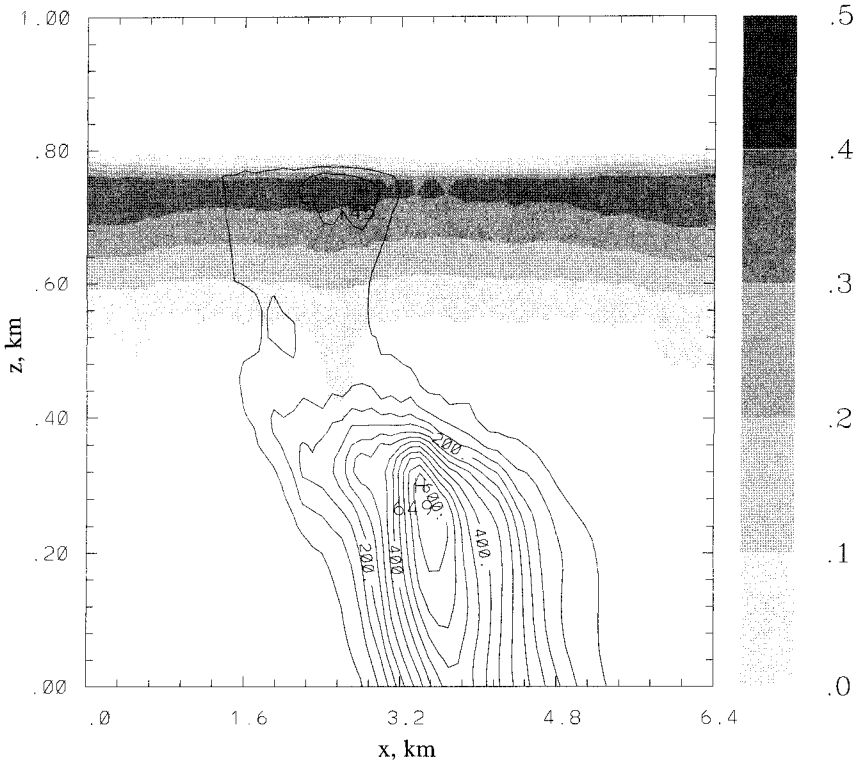

FIG. 11. Vertical cross sections (averaged over *x* direction) of liquid water content (shaded area) and passive tracer distributions (contours) at 30 min into A348_C1 simulation.

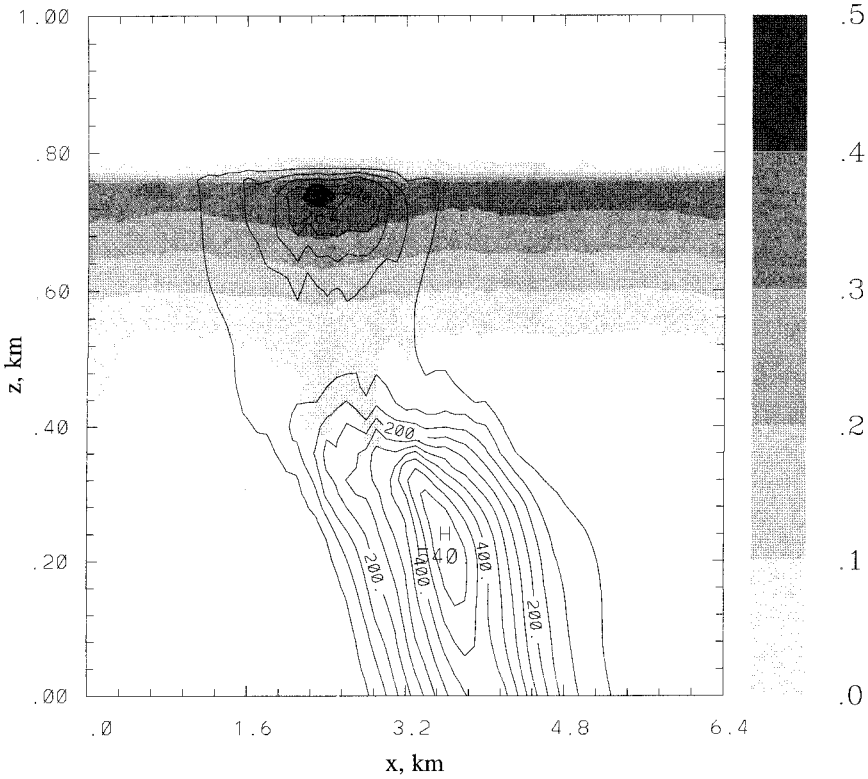

FIG. 12. Same as in Fig. 11, except for the simulation A348_C2.

Unauthenticated | Downloaded 09/14/24 02:12 PM UTC

TABLE 1. Specification of experiments and air parcel statistics. Here, T_{scl} denotes the temperature in the subcloud layer, while ΔT_{stl} gives the temperature jump across the subcloud transitional layer (STL).

			Percentage of air parcels above STL (min)		
Experiment	T_{scl} (K)	ΔT_{stl} (K)	$t = 10$	$t = 20$	$t = 30$
A348_B1	290.5	0.6	0	7.8	11.7
A348_C1	290.4	0.7	0	6.4	8.6
A348_C2	290.2	0.9	0	10.7	17.1
A348_C3	289.9	1.1	0	7.1	111.2
A348_C4	289.7	1.3	0	4.7	9.5

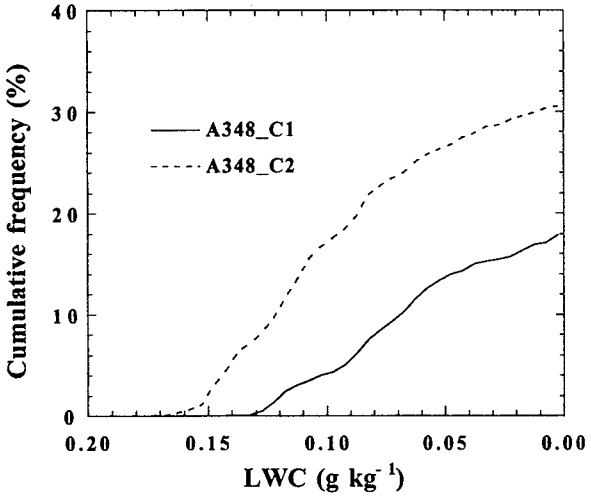

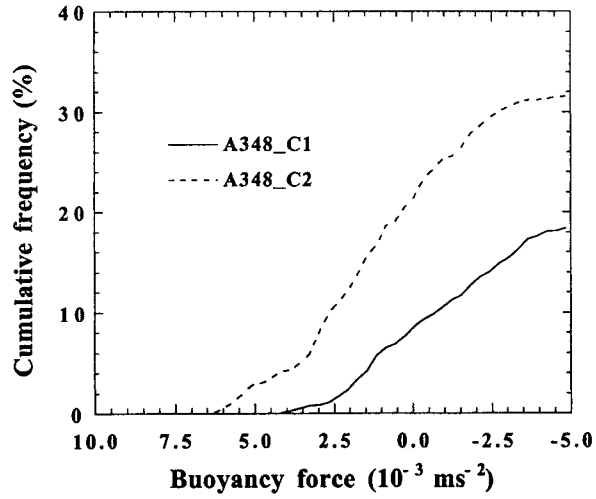

FIG. 13. Cumulative frequency of air parcels at $z = 400$ m as a percentage of the total number of parcels released at the surface with LWC (top) or buoyancy force (bottom) exceeding the given value.

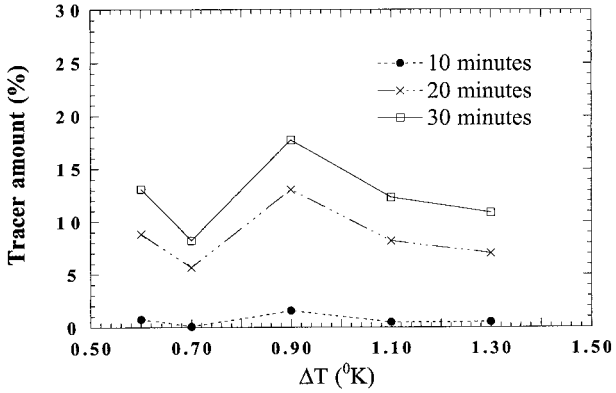

FIG. 14. Passive tracer accumulated above subcloud transitional layer (STL) at 10, 20, and 30 min as a function of the temperature jump across the STL.

sea surface temperature region, the results will be different. The stable subcloud transitional layer may or may not disintegrate depending on the relationship between the sea surface potential temperature and the mean potential temperature below and above the stable subcloud transitional layer. If the surface potential temperature is larger than the potential temperature in the upper half of the boundary layer, the situation will be similar to that of the constant heat flux. On the other hand, if the surface potential temperature is larger than that of the lower half of the boundary layer, but smaller than that of the upper half, the boundary layer may reach a quasi-steady state with a diminished surface heat flux that will maintain a somewhat weakened stable subcloud transitional layer. These and other scenarios affecting the boundary layer stability and, thus, transport of the ship effluent or other substance in the boundary layer warrant further investigation.

Acknowledgments. We would like to express our gratitude to the anonymous reviewers for their thorough review and numerous helpful suggestions. We would also like to thank Bob Bluth for giving us the opportunity to participate in the MAST experiment. This research was supported by the ONR Grants N00014-96-1-0687 and N00014-96-1-1112, by the Environmental Sciences Division of the U.S. Department of Energy (through Battelle PNL Contract 144880-A-Q1 to the Cooperative Institute for Mesoscale Meteorological Studies) as part of the Atmospheric Radiation Measurement Program, and by the NOAA OGP Grant NA37RJ0203.

REFERENCES

Albrecht, B. A., 1989: Aerosols, cloud microphysics, and fraction cloudiness. *Science,* **245,** 1227–1230.

Deardorff, J. W., 1980: Stratocumulus-capped mixed layers derived from a three-dimensional model. *Bound.-Layer Meteor.,* **18,** 495–527.

Unauthenticated | Downloaded 09/14/24 02:12 PM UTC

——, and G. E. Willis, 1975: A parameterization of diffusion into the mixed layer. *J. Appl. Meteor.,* **14,** 1451–1458.
Emanuel, K. A., 1994: *Atmospheric Convection.* Oxford University Press, 580 pp.
Khairoutdinov, M. F., and Y. L. Kogan, 1999: A large eddy simulation model with explicit microphysics: Validation against aircraft observations of a stratocumulus-topped boundary layer. *J. Atmos. Sci.,* **56,** 2115–2131.
Lamb, R. G, 1982: Diffusion in the convective boundary layer. *Atmospheric Turbulence and Air Pollution Modeling*, F. T. M. Nieuwstadt and H. van Dop, Eds., Kluwer, 159–339.
Lilly, D. K., 1962: On the numerical simulation of buoyant convection. *Tellus,* **14,** 148–172.
Moeng, C.-H., 1984: A large-eddy simulation model for the study of planetary boundary layer turbulence. *J. Atmos. Sci.,* **41,** 2052–2062.
——, 1986: Large-eddy simulation of a stratus-topped boundary layer. Part I: Structure and budgets. *J. Atmos. Sci.,* **43,** 2886–2900.
Porch, W. M., C. J. Kao, T. G. Kyle, and R. G. Kelley, 1989: Ship trail/cloud dynamic effects from Apollo-Soyuz photograph July 16, 1975. Preprints, *Symp. on the Role of Clouds in Atmospheric Chemistry and Global Climate,* Anaheim, CA, Amer. Meteor. Soc., 161–164.
Radke, L. F., J. H. Lyons, P. V. Hobbs, and J. E. Coakley, 1988: In situ measurements of ''ship tracks.'' Preprints, *10th Int. Cloud Physics Conf.,* Vol. 1, Bad Homburg, Germany, Amer. Meteor. Soc., 121–123.
Slingo, A., and H. M. Schrecker, 1982: On the shortwave radiative properties of stratiform water clouds. *Quart. J. Roy. Meteor. Soc.,* **108,** 407–426.
Smolarkiewicz, P. K., and W. W. Grabowski, 1990: The multi-dimensional positive definite advection transport algorithm: Nonoscillatory option. *J. Comput. Phys.,* **86,** 355–375.
Tremback, C. J., J. Powell, W. R. Cotton, and R. A. Pielke, 1987: The forward-in-time upstream advection scheme: Extension to higher orders. *Mon. Wea. Rev.,* **115,** 540–555.
Wyant, M. C., C. S. Bretherton, H. A. Rand, and D. E. Stevens, 1997: Numerical simulation and a conceptual model of the stratocumulus to trade cumulus transition. *J. Atmos. Sci.,* **54,** 168–192.

Unauthenticated | Downloaded 09/14/24 02:12 PM UTC